Advanced Journal of Chemistry, Section A

Journal homepage: www.ajchem-a.com

Original Research Article

Isolation and Evaluation of 8-Deoxygartanin from *Garcinia mangostana* as Dual EGFR/VEGFR-2 Inhibitors: Integrated *In Vitro* and Molecular Dynamics Approaches

Fera Kurniadewi[1]*, Irma Ratna Kartika[1], Elsa Vera Nanda[1], Hanhan Dianhar[1], Bina Permana[1], Naila Mushofa[1], Andi Fatimah Azzahra[1], Ade Danova[2], Elvira Hermawati[2]

[1]*Chemistry Study Program, Universitas Negeri Jakarta, Jakarta, Indonesia*
[2]*Organic Chemistry Division, Department of Chemistry, Faculty of Mathematics and Natural Sciences, Institut Teknologi Bandung, Jl. Ganesha No. 10, Bandung 40132, Indonesia*

A R T I C L E I N F O

Article history

Submitted: 2025-11-03
Revised: 2025-12-26
Accepted: 2026-01-05
ID: AJCA-2512-1992
DOI: **10.48309/AJCA.2026.563858.1992**

K E Y W O R D S

Xanthones
Garcinia mangostana
Tyrosine kinase inhibitor
Structure-activity relationship
Molecular dynamics
Dual inhibitor

A B S T R A C T

Despite advances in cancer therapy, severe side effects and drug resistance highlight the need for safer multi-target strategies. Targeting multiple receptor tyrosine kinases has emerged as a rational approach, and natural products, particularly xanthones from *Garcinia mangostana*, offer structurally diverse scaffolds with promising anticancer potential. This study presents an *in vitro* evaluation of three xanthones: 8-deoxygartanin (**1**), gartanin (**2**), and garcinone B (**3**) evaluated against epidermal growth factor receptor (EGFR) and vascular endothelial growth factor receptor-2 (VEGFR-2/KDR). Among the tested compounds, 8-deoxygartanin (1) exhibited the strongest dual inhibitory activity, with 78% and 51% inhibition of VEGFR-2 and EGFR, respectively, at 10 µM. Molecular docking analysis indicated that compound (**1**) binds to the active pockets of both kinases primarily through hydrophobic interactions. Furthermore, molecular dynamics simulations confirmed the stability of compound (**1**)-protein complexes over 500 ns in an aqueous environment. Structure-activity relationship (SAR) analysis revealed that prenylation and the specific distribution of hydroxyl and methoxy groups significantly influenced potency and selectivity. Comparison with mangostin-type analogues further underscored the superior profile of compound (**1**). This study provides novel mechanistic insights into *Garcinia*-derived xanthones and highlights 8-deoxygartanin as a promising scaffold for the rational design of dual EGFR/KDR-targeting anticancer agents.

* Corresponding author: Kurniadewi, Fera
✉ E-mail: fera@unj.ac.id

GRAPHICALABSTRACT

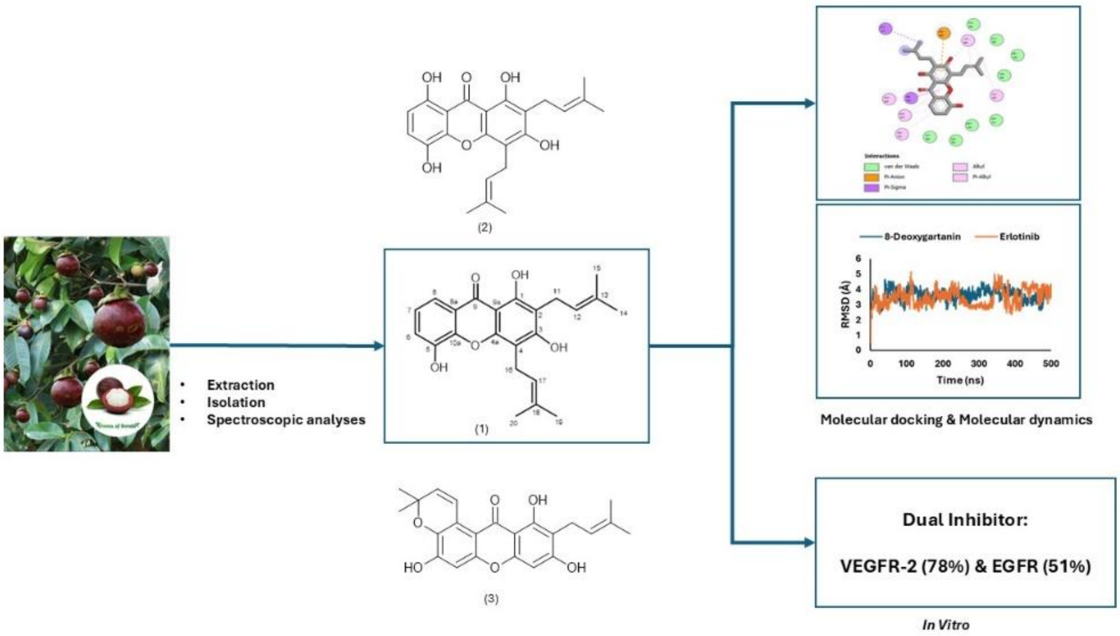

Introduction

Cancer remains one of the leading global health burdens, with over 19 million new cases and nearly 10 million deaths in 2020, and projections rising to 30 million cases by 2040 [1]. Despite advances in conventional therapies such as chemotherapy, radiotherapy, and surgery, these treatments often suffer from severe side effects, toxicity, and the emergence of drug resistance [2,3]. These limitations underscore the urgent need for safer and more effective therapeutic strategies. Receptor tyrosine kinases (RTKs), particularly epidermal growth factor receptor (EGFR) and vascular endothelial growth factor receptor-2 (VEGFR-2/KDR), are critical drivers of tumor proliferation, survival, and angiogenesis [4–6]. Dual inhibition of EGFR and VEGFR-2 has therefore emerged as a rational approach to simultaneously suppress tumor growth and vascularization. Several synthetic scaffolds, including oxadiazole, indole, and benzimidazole hybrids, have been reported as promising dual EGFR/VEGFR-2 inhibitors, demonstrating the utility of structure–activity relationship (SAR)-guided optimization [7–12]. Natural products remain a rich source of anticancer agents, with xanthones from *Garcinia mangostana* garnering significant attention. These compounds exhibit diverse biological activities, including anticancer [13–18], antioxidant [19–22], and anti-inflammatory effects [23–25]. Importantly, substitution patterns, such as hydroxylation and prenylation, have been shown to influence kinase inhibition and cytotoxicity [26,27]. At the same time, other studies highlighted xanthones for their potential to modulate EGFR in glioblastoma models and as synthetic analogues that act as topoisomerase II inhibitors [26]. Collectively, these findings emphasize the versatility of the xanthone scaffold in anticancer drug discovery. The previous studies demonstrated that α-mangostin (**4**) and β-mangostin (**5**) exert moderate inhibitory effects on EGFR and VEGFR-2, with activities of approximately 29–30% and docking energies of –8.2 to –8.4 kcal/mol [27]. In addition, 2,8-diisoprenyl-1,3-dihydroxy-6,7-dimethoxyxanthone (**6**) isolated from *G. mangostana* twigs showed similarly reduced activity, underscoring the influence of prenylation and methoxylation patterns on kinase binding affinity. These findings highlight both the potential and limitations of mangostin-type xanthones, suggesting the need to explore other *Garcinia*-derived analogues with distinct substitution patterns.

In this context, xanthones such as 8-deoxygartanin (**1**), gartanin (**2**), and garcinone B (**3**) are less frequently studied than mangostin analogues, despite reports of their antitumor, antiviral, and neuroprotective properties [28,29]. Nevertheless, the potential of compounds **1**-**3** as dual EGFR/VEGFR-2 inhibitors remains under-investigated. No study has systematically combined *in vitro* kinase assays with *in silico* docking and molecular dynamics to evaluate these compounds and compare them with mangostin-type xanthones. The present study addresses this gap by assessing the inhibitory activity of compounds **1**–**3** and performing comparative SAR analysis. This integrated approach provides novel mechanistic insights into xanthone–kinase interactions, highlighting *Garcinia*-derived xanthones as promising scaffolds for the rational design of dual-target anticancer agents.

Experimental

Materials and methods

General experimental procedure

UV–Vis spectra were recorded on a Shimadzu UV-1900i spectrophotometer, FT-IR spectra on a Shimadzu IR Spirit-Q-ATR, ^{1}H (500 MHz) and ^{13}C (125 MHz) NMR spectra on an Agilent DD2 spectrometer, and HRMS data on a Waters LCT Premier XE ESI-TOF instrument. VLC and CPC were used for chromatographic separations on Merck silica gel 60 GF254 (art. 7731, 7749). TLC analyses were performed on 0.25 mm pre-coated Kieselgel 60 GF254 plates (Merck). Detection was achieved using UV irradiation followed by heating after treatment with a 20% MeOH–H_2SO_4 solution. All solvents and reagents were of analytical grade and purchased from Merck, Germany. Tyrosine kinase inhibitory activity was assessed using the Promega Kinase Selectivity Profiling System according to previously reported protocols [27,30,31].

Material

Samples of mangosteen pericarp and leaves (*G mangostana*) were sourced from Mekarsari Fruit Garden, West Java Province, Indonesia, in May 2023. A voucher specimen (No. 2023048) has been preserved in the herbarium of Universitas Negeri Jakarta for documentation.

Extraction and isolation

The air-dried leaves of *G mangostana* (2 kg) were ground into a fine powder and extracted twice with ethyl acetate (2 × 3.5 L) at room temperature. The solvent was removed under reduced pressure, affording 55 g of extract. The ethyl acetate (EtOAc) extract was subjected to vacuum liquid chromatography (VLC) on silica gel using a stepwise gradient of *n*-hexane to acetone, yielding ten major fractions designated A–J. Fraction B (7.8 g) was further fractionated by VLC utilizing a gradient of *n*-hexane and ethyl acetate, resulting in twelve fractions (B1–B12). Fraction B9 (0.453 g) was subsequently purified by radial chromatography over silica gel, eluted with chloroform/*n*-hexane (6:4), affording ten fractions (B91–B910). Compound **1** (55 mg) was isolated from fraction B91. Powdered pericarps of *G. mangostana* (3.5 kg) were macerated with EtOAc, and the combined filtrates were concentrated under reduced pressure to give 14 g of crude extract. The extract was fractionated by vacuum liquid chromatography (VLC) on silica gel using n-hexane–EtOAc gradients (9:1 to 0:10), affording eight main fractions (A–H). Fraction B (3.7 g) was repeatedly purified by VLC, followed by Sephadex LH-20 chromatography (eluted with methanol), yielding compound **2** (11.4 mg). Fraction F (0.689 g) was separated by radial chromatography with n-hexane–acetone (7:3), and subfraction F9 (263.1 mg) was further purified by radial chromatography (n-hexane–acetone, 8:2) to afford fraction F9.4 (94.2 mg). Preparative TLC using chloroform–EtOAc (7:3) yielded compound **3** (6.8 mg). The identities of all isolated compounds were confirmed by UV, IR, MS, and NMR analyses, with references. New methods or substantially modified methods may be described in sufficient detail.

The selected spectral data

*8-deoxygartanin (**1**)*

Yellowish solid. UV (MeOH) λ_{max} (nm): 243, 256, 310 nm; IR (KBr) ν_{max} (cm^{-1}): 3,364, 2,968, 2,968, 2,912, 1,717, 1,617, 1,577, and 1,097; ^{1}H- and ^{13}C-NMR ($CDCl_3$) see Table 1; HRESITOF–MS (positive mode) m/z ($[M+H]^+$ 381.1700, (calcd. $[M+H]^+$ for $C_{23}H_{25}O_5$ 381.1702).

*Gartanin (**2**)*

Yellowish solid. UV (MeOH) λ_{max} (nm): 242, 349 nm; IR (KBr) ν_{max} (cm^{-1}): 3,219, 1,653, and 1,260; ^{1}H- and ^{13}C-NMR ($CDCl_3$) see Table 2; HRESITOF–MS (positive mode) m/z ($[M+H]^+$ 395.1493, (calcd. $[M+H]^+$ for $C_{23}H_{23}O_6$ 395.1495).

*Garcinone B (**3**)*

Yellowish solid. UV (MeOH) λ_{max} (nm): 245, 265, 333, and 370 nm; IR (KBr) ν_{max} (cm^{-1}): 3,477, 2,954, 2,856, 1,650, 1,598, 1,491, and 1,289; ^{1}H- and ^{13}C-NMR ($CDCl_3$) see Table 3; HRESITOF–MS (positive mode) m/z ($[M+H]^+$ 397.1641, (calcd. $[M+H]^+$ for $C_{23}H_{25}O_6$ 397.1651).

Molecular modeling simulation

8-Deoxygartanin (**1**) was docked to the binding pocket of EGFR and VEGFR-2 using Autodock Vina in PyRx V.1.1 [32,33] , with exhaustiveness of 32 and 9 poses per docked ligand. The docking protocol was validated by redocking the native ligand into the protein's binding site, yielding an RMSD ≤ 2 Å. The binding pocket locations for protein targets had dimensions 50 x 50 x 50 Å, such as EGFR (X: 21.470, Y: 0.636, and Z: 52.204 Å) and VEGFR-2 (X: -23.705, Y: 0.143, and Z: -10.598 Å). Docking results were analyzed and visualized in 2D and 3D using BIOVIA Discovery Studio Visualizer. Furthermore, molecular dynamics simulations were performed using YASARA Structure (v21.6.7) with the AMBER14 force field [34–37]. A series of preparations, including hydrogenation, optimization, and calibration, were carried out before the simulation. After minimizing the system's initial energy, the pH was set to 7.4, and the MD simulation was run at 298 K. The complex was placed in a water box with a size of 100.0 Å × 100.0 Å × 100.0 Å along the x-, y-, and z-axes. Periodic boundary conditions were then applied. Root-Mean-Square Deviation (RMSD) outputs were used to determine structural stability and rigidity. Additionally, the number of contacts in the solute and radius of gyration (Rg) was analyzed.

Results and Discussion

*Structure elucidation of compounds **1-3***

The structures of compounds **1-3** were elucidated by UV, IR, HRMS, and NMR (^{1}H, ^{13}C, and 2D) spectroscopic analyses, supported by comparison with literature data. Their chemical structures are presented in Figure 1. The ^{1}H and ^{13}C-NMR data are summarized in Tables 1-3, while key HMBC correlations confirming the substitution patterns are shown in Figures 2-4. For compound 1, the UV spectrum showed absorption maxima (λ_{max}) at 243, 256, and 310 nm, characteristic of xanthone. The IR spectrum also showed the maximum absorption at wavenumber (ν_{max}), as well as the prominent peaks of xanthone, including the hydroxyl group at 3,364 cm^{-1}, the conjugated carbonyl group at 1,717 cm^{-1}, and an aromatic band at 1,577 cm^{-1}. The ^{1}H-NMR spectrum (Table 1) exhibited a highly deshielded singlet at δ_H 13.33 ppm (1H, *s*), attributed to a chelated hydroxyl proton (1-OH), indicative of intramolecular hydrogen bonding with the adjacent carbonyl group, characteristic of xanthone derivatives [38]. In the aromatic region, three signals were observed: δ_H 7.70 (1H, dd, *J* = 7.9, 1.6 Hz, H-8), δ_H 7.38 (1H, dd, *J* = 7.9, 1.6 Hz, H-6), and δ_H 7.26 (1H, t, *J* = 7.9 Hz, H-7). These signals form an ABX pattern, consistent with a 1,2,3-trisubstituted benzene ring (ring B). The coupling constants confirm *ortho* and *meta* couplings, consistent with substitution at C-5 and C-8a, and the absence of a hydroxyl proton at C-8 distinguishes the compound from **2**, supporting its identification as 8-deoxygartanin (**1**). Two prenyl substituents were evident from olefinic triplets at δ_H 5.31 and 5.25 ppm, assignable to H-12 and H-17, along with benzylic methylene signals at δ_H 3.69 (2H, H-16) and δ_H 3.46 (2H, H-11). Four methyl singlets at δ_H 1.87, 1.80, 1.67, and 1.66 ppm (each 3H) further confirmed the presence of two prenyl groups. The ^{13}C-NMR spectrum displayed 26 distinct carbon signals, including a downfield resonance at δ_C 182.5 ppm, characteristic of a conjugated carbonyl (C-9). Oxygenated and substituted aromatic carbons were observed at δ_C 159.8 (C-1), 162.0 (C-3), 153.9 (C-4a), 147.6 (C-5), and 146.8 (C-10a) ppm. The methylene carbons of the prenyl substituents resonated at δ_C 22.8 (C-11) and 22.5 (C-16) ppm, while terminal methyl carbons appeared at δ_C 26.3, 26.2, 18.5, and 18.4 ppm. Taken together, the spectroscopic data unequivocally support the structure of the compound as 8-deoxygartanin (1-hydroxy-2,4-di(3-methyl-2-butenyloxy) xanthone [39], as shown in Figure 1.

Table 1. ^{1}H and ^{13}C-NMR data of compound **1** in $CDCl_3$

No.	δ_H (multiple, *J* in Hz) (ppm)	δ_C (ppm)	HMBC
1	-	158.8	-
2	-	109.3	-
3	-	161.1	-
4	-	105.5	-
4a	-	152.5	-
5	-	144.6	-
6	7.28 (1H, dd, *J*=7.8 & 1.6 Hz)	119.9	C8, C10a
7	7.22 (1H, t, *J*=7.9 Hz)	123.9	C5, C8a
8	7.75 (1H, dd, *J*=7.9 & 1.6 Hz)	117.0	C6, C9, C10a
8a	-	121.0	-
9	-	181.2	-
9a	-	103.4	-
10a	-	144.4	-
11	3.47 (2H, d, *J*=6.3 Hz)	21.8	C1, C2, C3, C12, C13
12	5.31 (1H, t, *J*=6.8 & 1.4 Hz)	121.3	C11, C14, C15
13	-	136.2	-
14	1.78 (3H, s, *J*=1.6 Hz)	26.0	C12, C13, C15
15	1.85 (3H, d, *J*=1.2 Hz)	18.1	C12, C13, C14
16	3.53 (2H, d, *J*=7.8 Hz)	22.2	C3, C4, C4a, C17, C18
17	5.25 (1H, t, *J*=6.9 & 1.4 Hz)	122.4	
18		133.7	
19		25.8	
20		18.08	
1-OH		-	
5-OH		-	
5-OH		-	

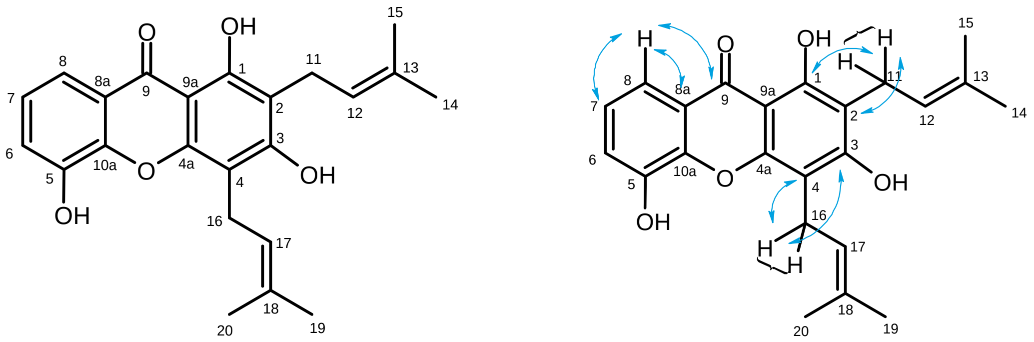

(a) (b)

Figure 1. (a) Structure of 8-deoxygartanin (**1**) and (b) selected HMBC correlations of compound **1**

The structure of compound **2** was elucidated as a xanthone derivative, based on detailed analysis of UV, IR, MS, and its ^{1}H- and ^{13}C-NMR spectra in $CDCl_3$. The UV spectrum showed absorption maxima (λ_{max}) at 242 and 349 nm, indicative of the xanthone chromophore. Correspondingly, the IR spectrum revealed the maximum absorption at wavenumber (λ_{max}) characteristic bands of xanthone, including a broad hydroxyl stretching vibration at 3,219 cm^{-1}, a conjugated carbonyl stretch at 1,653 cm^{-1}, and an aromatic C=C absorption at 1,260 cm^{-1}. The NMR spectrum showed that a highly deshielded carbonyl resonance at δ_C 185.9 (C-9) confirmed the xanthone backbone. Two chelated hydroxyl protons at δ_H 12.34 (1-OH) and 11.31 (8-OH) supported the presence of phenolic groups at C-1 and C-8, typical for xanthones. The aromatic region exhibited an *ortho*-coupled AB system at δ_H 7.31 (d, *J*=8.8 Hz, H-6) and 6.61 (d, *J*=8.8 Hz, H-7), consistent with a 1,2-disubstituted benzene ring (ring B). Two oxygenated prenyl units were identified from characteristic signals: methylene protons at δ_H 3.45 (H-11) and 3.67 (H-16), olefinic protons at δ_H 5.22 (H-12) and 5.27 (H-17) ppm, and allylic methyl singlets at δ_H 1.65–1.85 ppm. HMBC correlations of H-11 with C-1, C-2, and C-3 located the first O-prenyl group at C-2, while H-16 correlations with C-3, C-4, and C-4a confirmed the second O-prenyl group at C-4. All spectral features established the structure as 1,8-dihydroxy-2,4-di(3-methyl-2-butenyloxy) xanthone (gartanin) (**2**), in complete agreement with literature data [40], as shown in Figure 2.

Comprehensive spectroscopic analysis (UV, IR, MS, ^{1}H-NMR, and ^{13}C-NMR) confirmed that compound **3** belongs to the xanthone class. The UV spectrum showed absorption maxima (λ_{max}) at 245, 265, 333, and 360 nm, typical of xanthone chromophores with extended conjugation. The IR spectrum showed maximum absorption at wavenumber (λ_{max}) at 3,477 cm^{-1} (hydroxyl group), 1,650 cm^{-1} (conjugated carbonyl), and 1,598 cm^{-1} (aromatic C=C), further substantiating the presence of the xanthone skeleton. The spectra establish a xanthone skeleton: a downfield carbonyl at δC 182.8 (C-9) and a strongly chelated phenolic proton at δ_H 13.79 (1-OH). The aromatic region shows two isolated singlets at δ_H 6.43 (H-4) and 6.76 (H-5). HMBC from H-4 → C-3, C-4a, C-2, C-9a defines its position on ring A, while H-5 → C-6, C-8a, C-7, C-10a places it on ring B, indicating heavy substitution elsewhere.

Table 2. ^{1}H-NMR and ^{13}C-NMR data of **2** in $CDCl_3$

No.	δ_H (multiple, *J* in Hz) (ppm)	δ_C (ppm)	HMBC
1-OH	12.34 (s)	158.8	C-2, C-3, C-4a, C-9, C-9a, C-11
2		111.6	
3		162.5	
4		107.7	
4a		153.6	
5		138.09	
6	7.31 (d, *J*=8.8)	124.5	C-5, C-7, C-8, C-10a
7	6.61 (d, *J*=8.8)	109.9	C-5, C-6, C-8, C-8a
8	11.31 (s)	153.9	
8a		108.3	
9		185.92	
9a		101.8	
10a		145.07	
11	3.45 (d, *J*=5.3)	22.09	C-1, C-2, C-3, C-12, C-13
12	5.22	122.7	
13		132.5	
14	1.65 (s)	25.9	C-15, C-13, C-12
15	1.79 (s)	17.9	C-12, C-13, C-14
16	3.67 (d, *J*=5.3)	22.3	C-3, C-4, C-4a, C-17, C-18
17	5.27 (t, *J*=1.45)	122.9	
18		132.7	
19	1.85 (s)	18.1	C-17, C-18, C-20
20	1.65 (s)	25.9	C-17, C-18, C-19

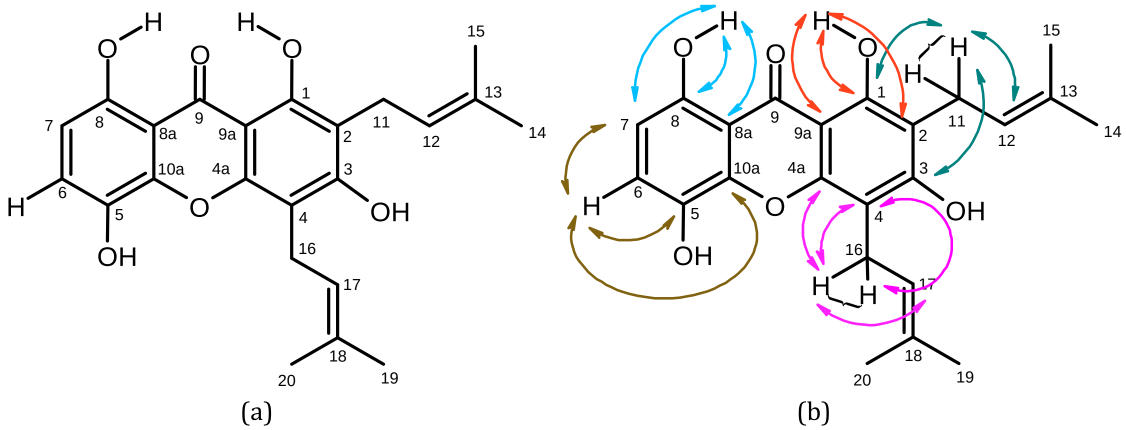

Figure 2. (a) Structure of gartanin (**2**) and (b) selected HMBC correlations of 2

A C-prenyl side chain is indicated by a benzylic methylene at δ_H 3.34 (2H, d, *J*=7.25, H-11; δ_C 22.0), an olefinic proton at δ_H 5.28 (t, H-12; δ_C 123.7), and two allylic methyl singlets at δ_H 1.78 (Me-14; δC 17.9) and 1.64 (Me-15; δC 25.9). HMBC H-11 → C-1, C-2, C-3, C-12, C-13 anchors this prenyl at C-2. A second isoprenyl unit has cyclized to a 2,2-dimethyl-2H-pyran (chromene) ring fused to the aromatic system: *trans*-olefinic protons δ_H 8.05 (d, *J*=10.2, H-16; δC 121.9) and 5.87 (d, *J*=10.2, H-17;

δ_C 132.9), a tertiary oxygenated carbon δ_C 76.4 (C-18), and gem-dimethyl singlets δ_H 1.44 (Me-19/Me-20; δC 27.1 each). HMBC H-17 → C-8, C-7, C-19, C-20 and H-16 → C-18, C-7 locate the pyran annulation across C-7–C-8. Together with the chelated 1-OH, these correlations define the structure as garcinone B: a prenylated-pyranoxanthone bearing a C-prenyl at C-2 and a 7,8-annulated 2,2-dimethyl-2*H*-pyran ring, entirely consistent with literature data for garcinone B (**3**) [41], as shown in Figure 3.

Table 3. ^{1}H-NMR and ^{13}C-NMR data of 3 in Acetone-d_6

No.	δ_H (multipl, *J* in Hz) (ppm)	δ_C (ppm)	HMBC
1-OH	13.79 (1H, s)	-	C1, C2, C9a
1	-	161.4	-
2	-	110.9	-
3	-	163.6	-
4	6.43 (1H, s)	93.3	C3, C4a, C2, C9a
4a	-	154.3	
5	6.76 (1H, s)	103.4	C6, C8a, C7, C10a
6	-	155.9	-
7	-	139.4	-
8	-	120.5	-
8a	-	106.5	-
9	-	182.8	-
9a	-	103.0	-
10a	-	154.3	-
11	3.34 (2H, d, *J*= 7.25 Hz)	22.0	C3, C1, C13, C12, C2
12	5.28 (1H, t)	123.7	C14, C15
13	-	131.2	-
14	1.78 (3H, s)	17.9	C12, C13, C15
15	1.64 (3H, s)	25.9	C12, C13, C14
16	8.05 (1H, d, *J* = 10.2 Hz)	121.9	C18, C7
17	5.87 (1H, d, *J* = 10.2 Hz)	132.9	C8, C7, C19, C20,
18	-	76.4	-
19	1.44 (3H. s)	27.1	C7, C18, C20
20	1.44 (3H, s)	27.1	C7, C18, C19

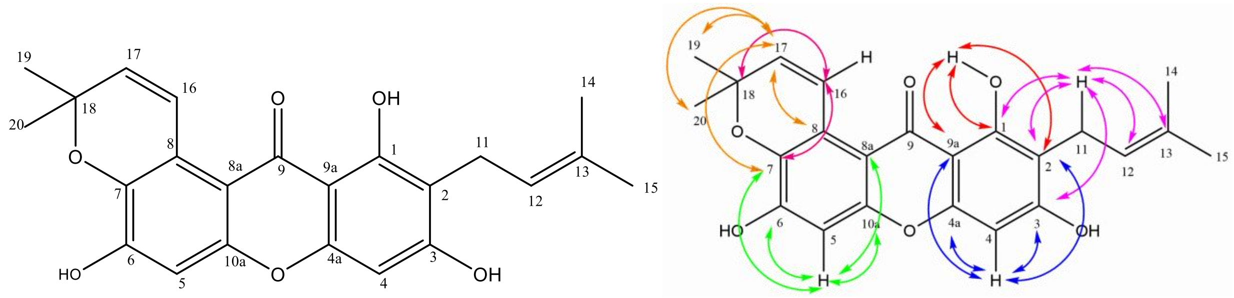

(a) (b)

Figure 3. (a) Structure of garcinone B (**3**) and (b) selected HMBC correlations of **3**

The NMR spectra showed that the absence of a hydroxyl signal at C-8, together with diagnostic HMBC correlations from H-11 to C-2/C-3/C-12 and from H-16 to C-3/C-4/C-4a, confirming the presence of two O-prenyl substituents at C-2 and C-4. In compound **2**, chelated hydroxyl protons at δ_H 12.34 (1-OH) and 11.31 (8-OH) supported the presence of phenolic groups at C-1 and C-8, while HMBC correlations located two O-prenyl groups at C-2 and C-4. In compound **3**, characteristic signals of a 2,2-dimethyl-2H-pyran ring fused at C-7–C-8 established its identity as a pyranoxanthone derivative. Having confirmed the structures of isolated compounds **1**–**3** as 8-deoxygartanin, gartanin, and garcinone B, their inhibitory activities against EGFR and KDR were subsequently evaluated to establish correlations between structural features and kinase inhibition. The inhibitory activities of compounds **1-3** against EGFR and KDR were assessed and compared with those of erlotinib, a reference inhibitor (Table 4).

Among the tested xanthones, **1** exhibited the strongest dual inhibition, with 51% inhibition of EGFR and 78% inhibition of KDR. compound **2** showed only weak inhibition (<20%), while compound **3** displayed intermediate activity. Erlotinib, as expected, exhibited complete inhibition of EGFR and strong activity against KDR, validating the assay. These results highlight that removal of the C-8 hydroxyl group, as in compound **1**, markedly enhanced dual inhibitory activity. In addition to EGFR and KDR, the compounds were tested against a broader kinase panel including HER2, HER4, IGF1R, InsR, PDGFRα, and PDGFRβ. The complete data are provided in the Supplementary Information (Table S1). These results confirmed that compound **1** selectively inhibited EGFR and KDR, with minimal activity against other kinases, supporting its specificity as a dual-target inhibitor.

Molecular modeling

8-Deoxygartanin (**1**) inhibited EGFR and VEGFR-2 with 51% and 78% inhibition at 10 μM, respectively. To further this study, molecular docking and dynamics simulation were performed on 8-deoxygartanin (**1**) to evaluate interactions and complex stability between the inhibitor and the protein in the binding pocket. The entire docking process was validated by redocking the native ligand, yielding an RMSD ≤ 2.0 Å (26), as shown in Figure 4.

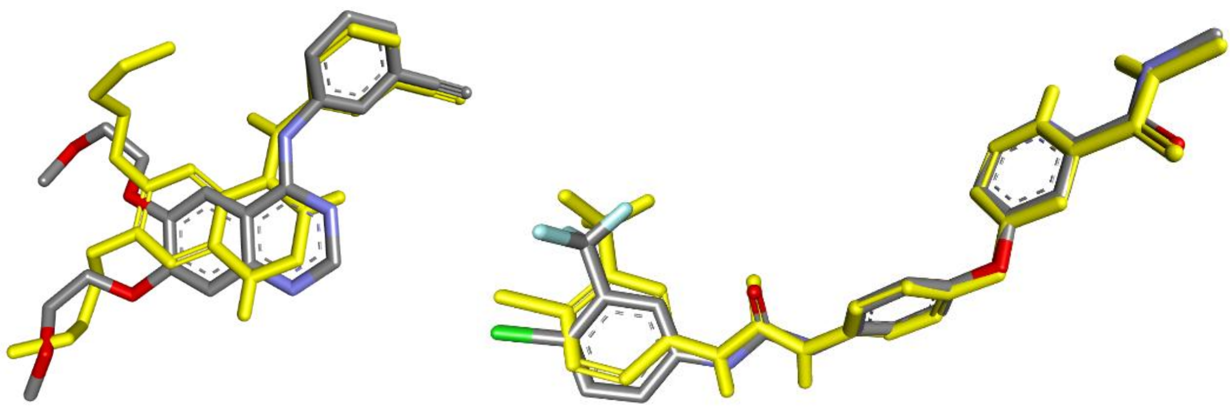

(a) (b)

Figure 4. Validation of the docking method (a) RMSD Erlotinib: 1.770 Å, (b) RMSD Sorafenib: 0.557 Å

Table 4. Inhibitory activity of compounds **1–3** and erlotinib against EGFR and VEGFR-2

Compound	Concentration (µM)	% Inhibition (EGFR)[a]	% Inhibition (VEGFR-2)[a]
8-Deoxygartanin (**1**)	10	51	78
Gartanin (**2**)	10	2	17
Garcinone B (**3**)	10	11	No inhibition
Erlotinib	1	100	58

[a]*strong >80%, moderate; 20-60%, weak or not active<60%*

As shown in Figure 5a, b, the 2D visualization of 8-deoxygartanin (**1**) targeting EGFR and VEGFR-2 revealed that most hydrophobic interactions occurred. Compound **1** with EGFR displayed a π-anion interaction with Asp855, π-σ interactions with the two amino residues of Phe723 and Val726, and several hydrophobic interactions with the five amino residues of Lys745, Leu788, Leu844, Ala743, and Leu718. Moreover, compound **1** with VEGFR-2 presented π-anion interaction with Asp1046 and several hydrophobic interactions with Leu1019, Ile892, Val898, Cys1045, Leu889, Val899, and Val916. Therefore, this result indicates that compound **1** could inhibit EGFR and VEGFR-2 via hydrophobic interactions at the binding sites. This result was similar to that of erlotinib and sorafenib, as shown in Figure 5c, d.

Furthermore, the complex stability of compound **1** with EGFR and VEGFR-2 was evaluated using molecular dynamics simulation by calculating root-mean-square displacement (RMSD), the number of atomic contacts (contacts), and the radius of gyration (Rg). The RMSD measures the stability of the complex between the inhibitor and the protein during simulation [42].

As shown in Figure 6a, b, the 8-deoxygartanin (**1**)-protein complexes fluctuated toward a stable state, with RMSD averages of 3.58 Å for EGFR and 3.70 Å for VEGFR-2 over 500 ns. Moreover, erlotinib and sorafenib showed RMSD averages of 3.45 Å with EGFR and 3.13 Å with VEGFR-2, respectively. The radius of gyration (Rg) value determines the compactness of the inhibitor-protein complex [43]. As shown in Figure 6c, d, the compactness of the compound **1**-EGFR complex showed a similar fluctuation to that of the erlotinib-EGFR complex. In addition, the compactness of compound **1** with VEGFR-2 was stabilized during a 500 ns simulation. Therefore, compound **1**–EGFR/VEGFR-2 complexes presented similar stability and compactness to those of the native ligand. Furthermore, atomic contacts play a key role in the inhibitor-protein binding affinity [44]. The number of contacts (contacts) of **1**-EGFR/VEGFR-2 exhibited similar results to those of the native ligand, as shown in Figure 6e, f. These results support the structural stability and compactness observed in the inhibitor-protein complexes in Figure 6a-d.

Comparative SAR analysis across six compounds

To rationalize the observed biological activities, a SAR analysis was conducted to correlate the functional group variations with their inhibitory potency. To better visualize the influence of substitution patterns on dual kinase inhibition, the SAR of six xanthones are summarized in Table 5 and Figure 7.

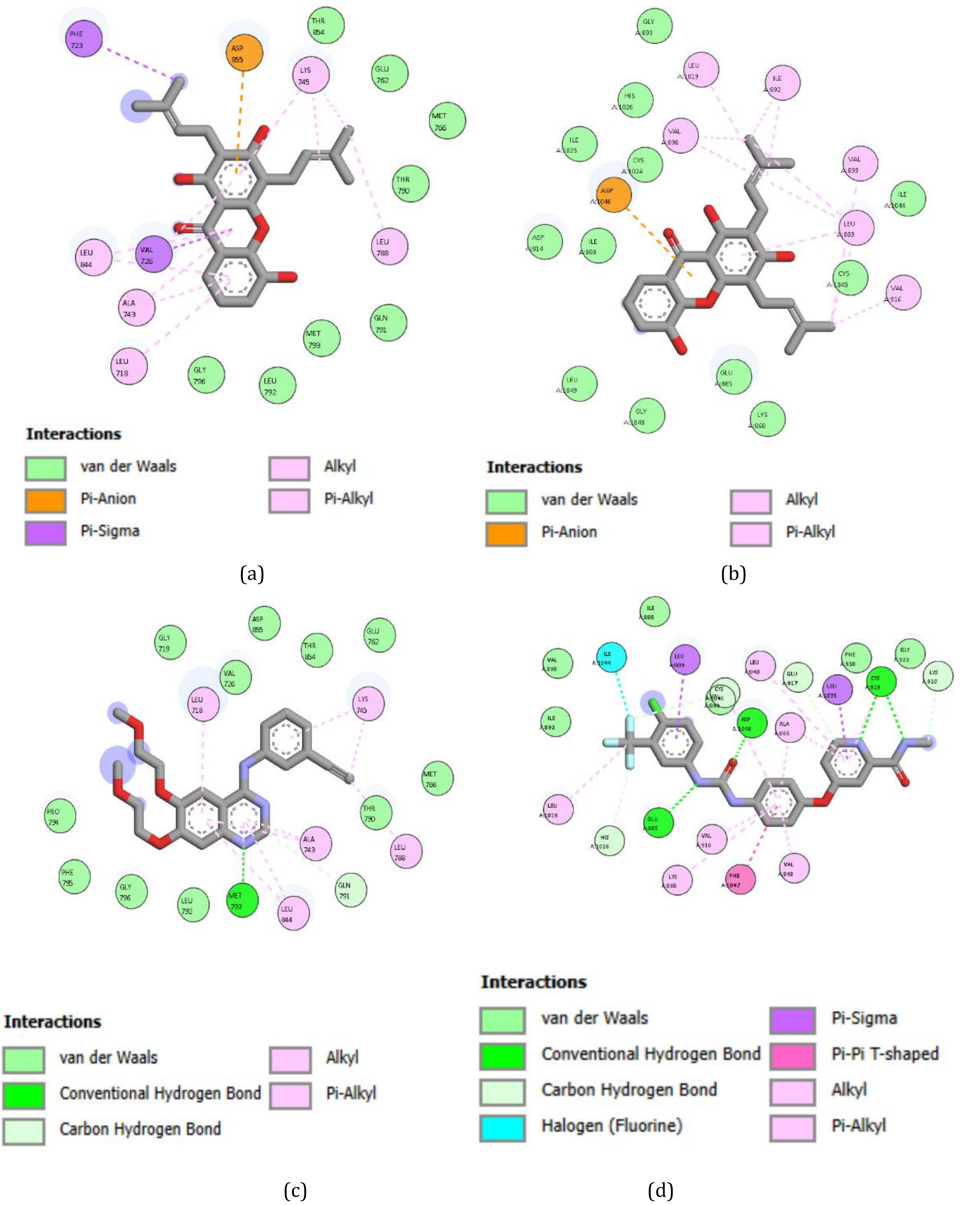

Figure 5. 2D interaction of inhibitor-protein complex: (a) 8-deoxygartanin-EGFR, (b) 8-deoxygartanin-VEGFR-2, (c) erlotinib-EGFR, and (d) sorafenib-VEGFR-2

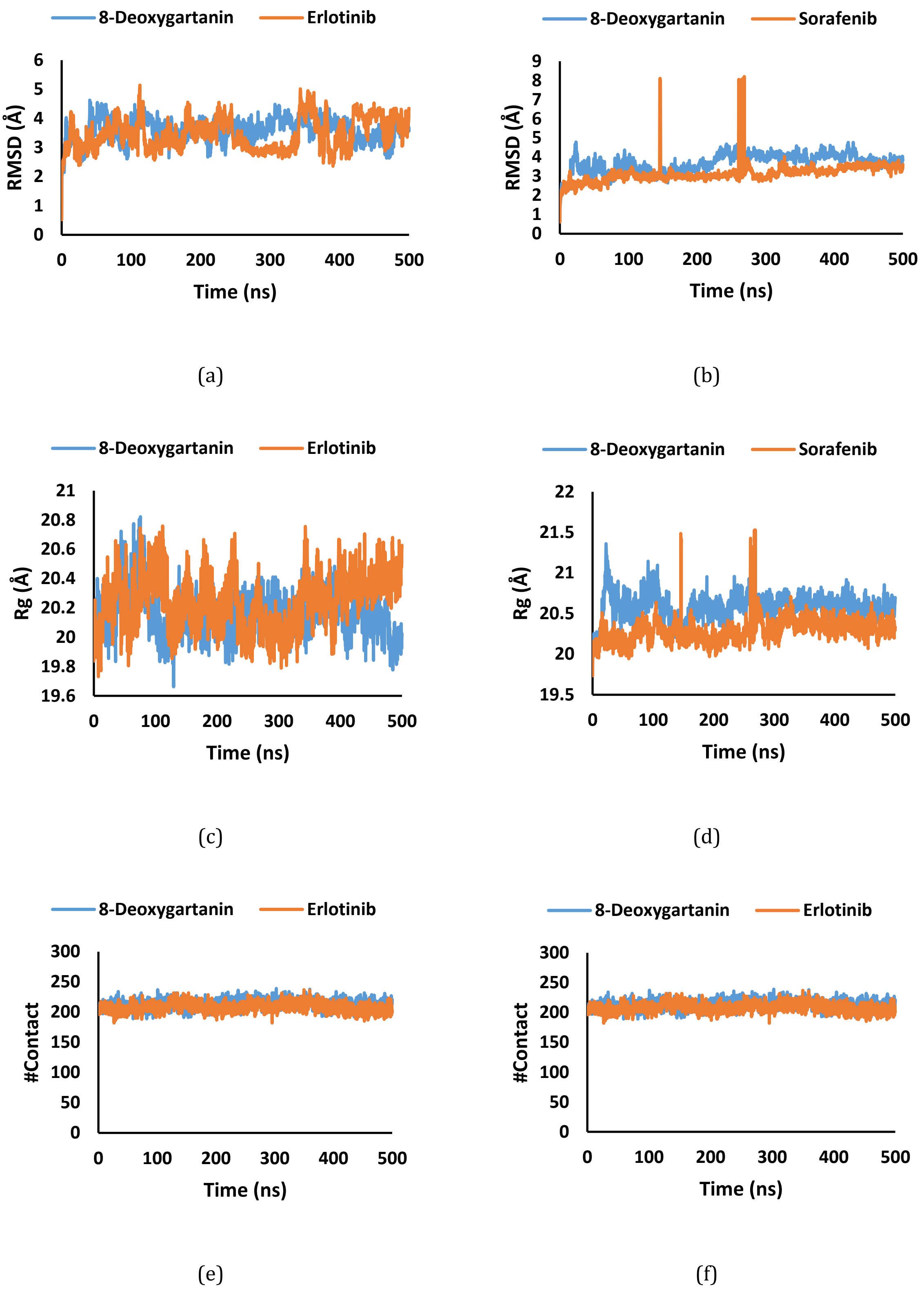

Figure 6. Result of molecular dynamics simulations for 500 ns. (a) RMSD-inhibitor with EGFR, (b) RMSD–inhibitor with VEGFR-2, (c) Rg-inhibitor with EGFR, (d) Rg-inhibitor with VEGFR-2, (e) # Contact–inhibitor with EGFR, and (f) # Contact–inhibitor with VEGFR-2

Table 5. SAR summary of Xanthones from *G mangostana*

Compound	C-1	C-3	C-6	C-7	C-8	EFGR activity	VEGFR-2 activity
α-Mangostin (**4**)	OH	OH	OMe	OMe	Prenyl	++	++
β-Mangostin (**5**)	OH	OH	OMe	OMe	OH	+	+
Gartanin (**2**)	OH	OH	OMe	Prenyl	Prenyl	+	+
8-Deoxygartanin (**1**)	OH	OH	OMe	Prenyl	H (no OH)	+++	+++
Garcinone B (**3**)	OH	OH	OMe	OMe	Prenyl	++	++
2,8-Diisoprenyl-1,3-dihydroxy-6,7-dimethoxyxanthone (**6**)	OH	OH	OMe	OMe	Prenyl	+	++

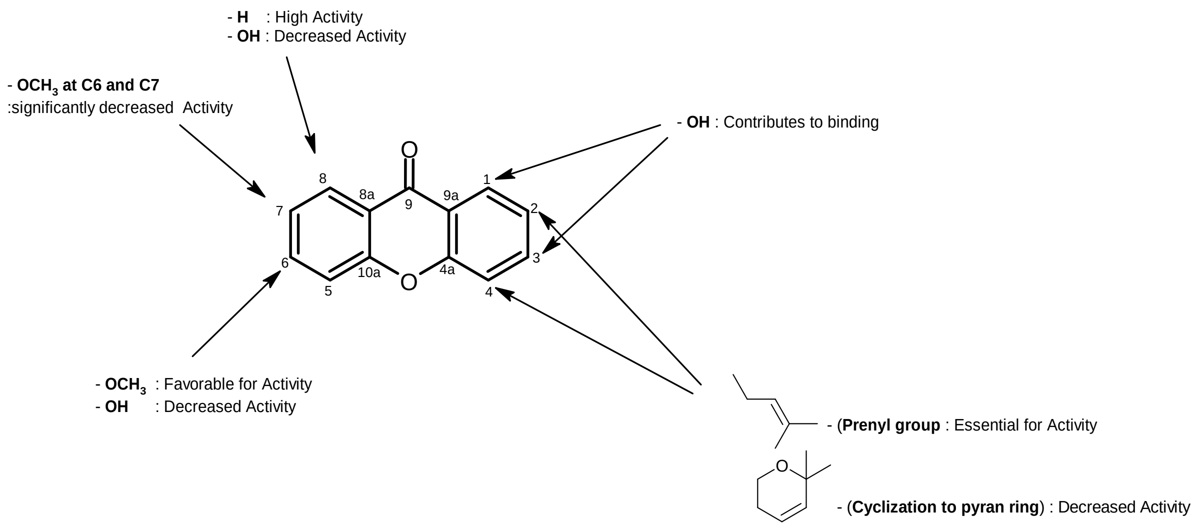

Figure 7. Integrated SAR summary for xanthone derivatives against tyrosine kinases

The comparative SAR analysis highlights that specific substitution patterns strongly influence dual inhibition toward EGFR and VEGFR-2. Among the tested xanthones, 8-deoxygartanin (**1**) exhibited the most potent dual inhibition (+++), whereas gartanin (**2**) and β-mangostin (**5**), which bear an additional hydroxyl group at C-8, showed significantly reduced activity (+). The fused chromene moiety of garcinone B (**3**) provided intermediate potency (++), likely due to steric constraints. The variation in biological activity can be rationalized by the distinct physicochemical properties conferred by the substituents on the xanthone skeleton. Critically, the absence of a hydroxyl group at C-8 in compound **1** appears to be a key structural determinant for potency**.** Chemically, the removal of this polar hydroxyl group significantly increases the scaffold's lipophilicity. This increased lipophilic character facilitates the molecule's penetration into the ATP-binding pockets of EGFR and VEGFR-2, which are predominantly hydrophobic in nature. In contrast, the presence of a hydrophilic C-8 hydroxyl group in compounds **2** and **5** increases polarity, which may impose a desolvation energy penalty—requiring energy to strip away water molecules before binding—and reduce compatibility with the hydrophobic cleft, thereby weakening receptor affinity. This observation aligns with the docking results, in which the more lipophilic core of 1 formed stronger hydrophobic interactions with key residues.

Furthermore, prenylation at C-2 and C-4 plays a crucial role in reinforcing hydrophobic anchoring. The flexible prenyl chains extend into the hydrophobic sub-pockets, optimizing van der Waals and π–π interactions that stabilize the ligand–receptor complex. Conversely, the fused chromene ring in garcinone B (**3**) introduces conformational rigidity; this lack of flexibility likely restricts the 'induced fit' adaptation required for optimal binding within the catalytic pocket, resulting in only moderate activity compared to the more flexible prenyl side chains of compound **1**. Consistent with these observations, previous reports on garcinone E have demonstrated comparable structure-function relationships, where a prenyl group enhances hydrophobic anchoring within the hinge region, and specific hydroxylation patterns act as hydrogen bond donors. Garcinone E was identified as a potent dual EGFR/VEGFR2 inhibitor with binding energies of approximately -9.3 and -9.1 kcal mol^{-1}, respectively [45]. The similar pharmacophoric arrangement observed in compound **1** suggests that both compounds utilize analogous molecular recognition strategies. Taken together, the SAR findings demonstrate that C-8 dehydroxylation acts as a structural trigger, increasing lipophilicity and enhancing dual EGFR/VEGFR-2 inhibition, while dual prenylation ensures the necessary hydrophobic stabilization. These structural insights establish compound **1** as a rational lipophilic scaffold for the future optimization of *Garcinia*-derived xanthones as dual tyrosine kinase inhibitors. Consequently, these findings highlight 8-deoxygartanin (**1**) as a compelling lead scaffold. Rational modifications, particularly strategies that reduce excessive polar hydroxylation or fine-tune the lipophilic prenyl side chains, could further optimize potency and bioavailability. This study, therefore, provides a verified structural framework for developing semi-synthetic xanthone derivatives with improved pharmacological profiles for targeted anticancer applications.

Conclusion

This study provides the first integrated evaluation of 8-deoxygartanin (**1**), gartanin (**2**), and garcinone B (**3**) as dual EGFR/VEGFR-2 inhibitors. Among the isolated compounds, 8-deoxygartanin (**1**) emerged as the most promising lead, displaying 78% and 51% inhibition against VEGFR-2 and EGFR, respectively, at 10 μM. Computational studies supported these findings; molecular docking revealed that the enhanced lipophilicity of compound **1** facilitates deep penetration into the hydrophobic binding pockets of both kinases. Furthermore, molecular dynamics simulations confirmed the stability of compound **1**–protein complexes in an aqueous environment over 500 ns, as evidenced by stable RMSD and compactness profiles. Crucially, SAR analysis identified C-8 dehydroxylation as a key structural determinant for potency, while dual prenylation provides essential hydrophobic anchoring. Collectively, these findings highlight 8-deoxygartanin as a valuable lipophilic scaffold for the rational development of next-generation dual-target anticancer agents.

Acknowledgement

This study was funded by a grant from the Directorate of Research, Technology, and Community Service, Directorate General of Higher Education, Research, and Technology, the Ministry of Higher Education, Science, and Technology, under contract number 5/UN39.14/C3/DT.05.00/PFR/PL/2025.

Gratitude is extended to Taman Buah Mekar Sari for samples and to the Integrated Chemistry Laboratory, FMIPA ITB, for NMR and assay support.

Disclosure Statement

No potential conflicts of interest were reported by the authors.

ORCID

Fera Kurniadewi:
https://orcid.org/0000-0002-3541-8103
Irma Ratna Kartika:
https://orcid.org/0009-0002-8845-8085
Elsa Vera Nanda:
https://orcid.org/0000-0002-4099-579X
Hanhan Dianhar:
https://orcid.org/0000-0001-8599-3619
Bina Permana:
https://orcid.org/0009-0007-7437-5509
Naila Mushofa:
https://orcid.org/0009-0006-9091-0885
Andi Fatimah Azzahra:
https://orcid.org/0009-0008-1624-3396
Ade Danova:
https://orcid.org/0000-0003-4716-1170
Elvira Hermawati:
https://orcid.org/0000-0002-5492-3316

References

[1] Bray, F., Laversanne, M., Sung, H., Ferlay, J., Siegel, R.L., Soerjomataram, I., Jemal, A. Global cancer statistics 2022: Globocan estimates of incidence and mortality worldwide for 36 cancers in 185 countries. *CA: A Cancer Journal for Clinicians*, **2024**, 74(3), 229-263.

[2] Rezaeianzadeh, O., Asghari, S., Tajbakhsh, M., Mohseni, M., Khalilpour, A. Synthesis, molecular docking, and anticancer evaluation of new azo-based sulfonamides against mcf 7 human breast cancer cell line. *Chemical Methodologies*, **2024**, 8, 329-350.

[3] Clancy, E. Acs report shows prostate cancer on the rise, cervical cancer on the decline. *Renal & Urology News*, **2023**, NA-NA.

[4] Abd Alkareem, T., Hassan, S., Abdalhadi, S. Breast cancer: Symptoms, causes, and treatment by metal complexes: A review. *Advanced Journal of Chemistry-Section B: Natural Products and Medical Chemistry*, **2023**, 5(4), 306-319.

[5] Carmeliet, P., Jain, R.K. Angiogenesis in cancer and other diseases. *Nature*, **2000**, 407(6801), 249-257.

[6] Shah, F.H., Nam, Y.S., Bang, J.Y., Hwang, I.S., Kim, D.H., Ki, M., Lee, H.W. Targeting vascular endothelial growth receptor-2 (vegfr-2): Structural biology, functional insights, and therapeutic resistance. *Archives of Pharmacal Research*, **2025**, 1-22.

[7] Mahmoud, M.A., Mohammed, A.F., Salem, O.I., Almutairi, T.M., Bräse, S., Youssif, B.G. Design, synthesis, and apoptotic antiproliferative action of new 1, 2, 3-triazole/1, 2, 4-oxadiazole hybrids as dual egfr/vegfr-2 inhibitors. *Journal of Enzyme Inhibition and Medicinal Chemistry*, **2024**, 39(1), 2305856.

[8] Mostafa, Y.A., Assoud, J.A., Desoky, A.Y., Mohamady, S., Mohamed, N.M., Salem, O.I., Almarhoon, Z.M., Bräse, S., Youssif, B.G. New series of 4, 6-diaryl pyrimidines: Facile synthesis and antiproliferative activity as dual egfr/vegfr-2 inhibitors. *Frontiers in Chemistry*, **2024**, 12, 1498104.

[9] Alsulaimany, M., Aljohani, A.K., Abd El-Sattar, N.E., Almadani, S.A., Alatawi, O.M., Alharbi, H.Y., Aljohani, M.S., Al-Shareef, A.H., Alghamdi, R., Tayeb, S.M. Dual vegfr-2 and egfrt790m inhibitors of phenyldiazenes: Anticancer evaluations, admet, docking, design and synthesis. *Future Medicinal Chemistry*, **2025**, 17(3), 287-300.

[10] Al-Wahaibi, L.H., Mohammed, A.F., Abdelrahman, M.H., Trembleau, L., Youssif, B.G. Design, synthesis, and biological evaluation of indole-2-carboxamides as potential multi-target antiproliferative agents. *Pharmaceuticals*, **2023**, 16(7), 1039.

[11] Alsfouk, A.A., Elkady, H., Hassan, S.M., Elgammal, W.E., Mahdy, H.A., Husein, D.Z., Amin, F.G., Hagras, M., Elkaeed, E.B., Metwaly, A.M. New thiadiazole-benzenesulfonamide hybrids as dual b-raf/vegfr-2 inhibitors with promising anti-hepatic cancer activity. *Chemical Biology & Drug Design*, **2025**, 106(1), e70156.

[12] Gadhave, R.V., Shelke, S.B., Biswas, A., Shastri, M.A., Pachauri, A.D., Ozarde, Y.S. Design, synthesis, and biological evaluation of novel 3-substituted-5-(3, 4-dimethoxy-phenyl)-3h-[1, 3, 4] oxadiazole-2-thione derivatives as anticancer agents. *Chemical Methodologies*, **2025**, 833-850.

[13] Ibrahim, S.R., Mohamed, G.A., Elfaky, M.A., Zayed, M.F., El-Kholy, A.A., Abdelmageed, O.H., Ross, S.A. Mangostanaxanthone vii, a new cytotoxic xanthone from garcinia mangostana. *Zeitschrift für Naturforschung C*, **2018**, 73(5-6), 185-189.

[14] Ibrahim, S.R., Abdallah, H.M., El-Halawany, A.M., Nafady, A.M., Mohamed, G.A. Mangostanaxanthone viii, a new xanthone from garcinia mangostana and its cytotoxic activity. *Natural Product Research*, **2019**, 33(2), 258-265.

[15] Wang, A., Liu, Q., Ye, Y., Wang, Y., Lin, L. Identification of hepatoprotective xanthones from the pericarps of garcinia mangostana, guided with tert-butyl hydroperoxide induced oxidative injury in hl-7702 cells. *Food & Function*, **2015**, 6(9), 3013-3021.
[16] Ong, Y.S., Murugaiyah, V., Goh, B.H., Khaw, K.Y. Bioactive xanthones from garcinia mangostana. *Plant-Derived Bioactives: Chemistry and Mode of Action*, **2020**, 281-300.
[17] Ortega, Y.T., Quintana, S.E., García-Zapateiro, L.A. Extraction of bioactive compounds from garcinia mangostana l., using green technologies: A comprehensive analysis. *Journal of Food Science and Technology*, **2025**, 1-12.
[18] Saraswathy, S.U.P., Lalitha, L.C.P., Rahim, S., Gopinath, C., Haleema, S., SarojiniAmma, S., Aboul-Enein, H.Y. A review on synthetic and pharmacological potential of compounds isolated from garcinia mangostana linn. *Phytomedicine Plus*, **2022**, 2(2), 100253.
[19] Suthammarak, W., Numpraphrut, P., Charoensakdi, R., Neungton, N., Tunrungruangtavee, V., Jaisupa, N., Charoensak, S., Moongkarndi, P., Muangpaisan, W. Antioxidant-enhancing property of the polar fraction of mangosteen pericarp extract and evaluation of its safety in humans. *Oxidative Medicine and Cellular Longevity*, **2016**, 2016(1), 1293036.
[20] Andrade, A.W.L., Machado, K.d.C., Machado, K.d.C., Figueiredo, D.D.R., David, J.M., Islam, M.T., Uddin, S.J., Shilpi, J.A., Costa, J.P. In vitro antioxidant properties of the biflavonoid agathisflavone. *Chemistry Central Journal*, **2018**, 12(1), 75.
[21] Jung, H.A., Su, B.N., Keller, W.J., Mehta, R.G., Kinghorn, A.D. Antioxidant xanthones from the pericarp of garcinia mangostana (mangosteen). *Journal of Agricultural and Food Chemistry*, **2006**, 54(6), 2077-2082.
[22] Suthammarak, W., Numpraphrut, P., Charoensakdi, R., Neungton, N., Tunrungruangtavee, V., Jaisupa, N., Charoensak, S., Moongkarndi, P., Muangpaisan, W. Antioxidant-enhancing property of the polar fraction of mangosteen pericarp extract and evaluation of its safety in humans. *Oxidative Medicine and Cellular Longevity*, **2016**, 2016(1), 1293036.
[23] Nhan, N.T., Nguyen, P.-H., Tran, M.H., Nguyen, P.-D.N., Tran, D.T., To, D.C. Anti-inflammatory xanthone derivatives from garcinia delpyana. *Journal of Asian Natural Products Research*, **2021**, 23(5), 414-422.
[24] Fan, X., Jia, Y., Guo, J., Yang, J., Li, D., Hua, H. Xanthones from garcinia pedunculata and garcinia nujiangensis and their anti-inflammatory activity. *Chinese Journal of Natural Medicines*, **2025**, 23(2), 225-233.
[25] Dewi, I.P., Aldi, Y., Ismail, N.H., Osman, C.P., Putra, P.P., Wahyuni, F.S. A new xanthone from garcinia cowa roxb. And its anti-inflammatory activity. *Journal of Ethnopharmacology*, **2025**, 343, 119380.
[26] Phang, Y.L., Zheng, C., Xu, H. Structural diversity and biological activities of caged garcinia xanthones: Recent updates. *Acta Materia Medica*, **2022**, 1(1), 72-95.
[27] Kurniadewi, F., Palah, L.M., Kartika, I.R., Nurjayadi, M., Hermawati, E., Danova, A. Isolation, characterization, and evaluation of xanthone derivatives from garcinia mangostana twigs as tyrosine kinase inhibitors with potential egfr selectivity. *Advanced Journal of Chemistry, Section A*, **2025**, 8(6), 1027-1042.
[28] Aukkanimart, R., Boonmars, T., Sriraj, P., Songsri, J., Laummaunwai, P., Waraasawapati, S., Boonyarat, C., Rattanasuwan, P., Boonjaraspinyo, S. Anthelmintic, anti-inflammatory and antioxidant effects of garcinia mangostana extract in hamster opisthorchiasis. *Experimental Parasitology*, **2015**, 154, 5-13.
[29] Luo, M., Liu, Q., He, M., Yu, Z., Pi, R., Li, M., Yang, X., Wang, S., Liu, A. Gartanin induces cell cycle arrest and autophagy and suppresses migration involving pi3k/akt/mtor and mapk signalling pathway in human glioma cells. *Journal of Cellular and Molecular Medicine*, **2017**, 21(1), 46-57.
[30] Kurniadewi, F., Aqilah, A.S., Kartika, I.R., Nurjayadi, M., Hermawati, E., Danova, A. Garciniaxanthone e and 12b-hydroxy-des-dgarcigerrin a from the tree bark garcinia dulcis and their inhibitory properties against receptor tyrosine kinases. *Jurnal Kimia Valensi*, **2024**, 10(1), 20-26.
[31] Mujahidin, D., Noviany, I., Hermawati, E., Danova, A., Heliawati, L., Syah, Y. Isolation and inhibition study of eryvarin d and e from the root barks of erythrina variegata against receptor tyrosine kinases. *Rasayan Journal of Chemistry*, **2024**, 17(3).
[32] Dallakyan, S., Olson, A.J. Small-molecule library screening by docking with PYRX. *Chemical Biology: Methods and Protocols*, **2014**, 243-250.
[33] Trott, O., Olson, A. Software news and update autodock vina: Improving the speed and accuracy of docking with a new scoring function. *Effic. Optim. Multithreading*, **2009**, 31, 455-461.
[34] Duan, Y., Wu, C., Chowdhury, S., Lee, M.C., Xiong, G., Zhang, W., Yang, R., Cieplak, P., Luo, R., Lee, T. A point-charge force field for molecular mechanics simulations of proteins based on condensed-phase quantum mechanical calculations. *Journal of Computational Chemistry*, **2003**, 24(16), 1999-2012.

[35] Krieger, E., Darden, T., Nabuurs, S.B., Finkelstein, A., Vriend, G. Making optimal use of empirical energy functions: Force-field parameterization in crystal space. *Proteins: Structure, Function, and Bioinformatics*, **2004**, 57(4), 678-683.

[36] Krieger, E., Vriend, G. New ways to boost molecular dynamics simulations. *Journal of Computational Chemistry*, **2015**, 36(13), 996-1007.

[37] Khatimah, H., Hermawati, E., Mulya, F., Abdjan, M.I., Kuamit, T., Danova, A. A new ursane-type pentacyclic triterpenoid from the tree bark of sandoricum koetjape: Antibacterial, dft, and molecular docking study. *International Journal of Molecular Sciences*, **2025**, 26(21), 10389.

[38] Chakthong, S., Chukaew, A., Saithong, S., Chusri, S., Limsuwan, S., Voravuthikunchai, S.P. Xanthones and coumarins from the twigs of mesua ferrea l. *Progress in Applied Science and Technology*, **2020**, 10(2), 37-42.

[39] Anggia, V., Bakhtiar, A., Arbain, D. The isolation of xanthones from trunk latex of garcinia mangostana linn. And their antimicrobial activities. *Indonesian Journal of Chemistry*, **2015**, 15(2), 187-193.

[40] Anggia, V., Bakhtiar, A., Arbain, D. The isolation of xanthones from trunk latex of garcinia mangostana linn. And their antimicrobial activities. *Indonesian Journal of Chemistry*, **2015**, 15(2), 187-193.

[41] Sanpa, S., Popova, M., Bankova, V., Tunkasiri, T., Eitssayeam, S., Chantawannakul, P. Antibacterial compounds from propolis of tetragonula laeviceps and tetrigona melanoleuca (hymenoptera: Apidae) from thailand. *PLoS One*, **2015**, 10(5), e0126886.

[42] Sabuakham, S., Nasoontorn, S., Kongtaworn, N., Rungrotmongkol, T., Silsirivanit, A., Pingaew, R., Mahalapbutr, P. Anilino-1, 4-naphthoquinones as potent mushroom tyrosinase inhibitors: In vitro and in silico studies. *Journal of Enzyme Inhibition and Medicinal Chemistry*, **2024**, 39(1), 2357174.

[43] Zhan, F., Ding, S., Xie, W., Zhu, X., Hu, J., Gao, J., Li, B., Chen, Y. Towards understanding the interaction of β-lactoglobulin with capsaicin: Multi-spectroscopic, thermodynamic, molecular docking and molecular dynamics simulation approaches. *Food Hydrocolloids*, **2020**, 105, 105767.

[44] Wang, D.D., Ou-Yang, L., Xie, H., Zhu, M., Yan, H. Predicting the impacts of mutations on protein-ligand binding affinity based on molecular dynamics simulations and machine learning methods. *Computational and Structural Biotechnology Journal*, **2020**, 18, 439-454.

[45] Li, J., Nie, X., Rangsinth, P., Wu, X., Zheng, C., Cheng, Y., Shiu, P.H.T., Li, R., Lee, S.M.Y., Fu, C. Structure and activity relationship analysis of xanthones from mangosteen: Identifying garcinone e as a potent dual EGFR and VEGFR2 inhibitor. *Phytomedicine*, **2024**, 122, 155140.

HOW TO CITE THIS ARTICLE

F. Kurniadewi, I.R. Kartika, E.V. Nanda, H. Dianhar, B. Permana, N. Mushofa, A.F. Azzahra, A. Danova, E. Hermawati. Isolation and Evaluation of 8-Deoxygartanin from *Garcinia mangostana* as Dual EGFR/VEGFR-2 Inhibitors: Integrated *In Vitro* and Molecular Dynamics Approaches. *Adv. J. Chem. A*, 2026, 9(6), 1014-1030.

DOI: 10.48309/AJCA.2026.563858.1992
URL: https://www.ajchem-a.com/article_238643.html